

PAPER • OPEN ACCESS

Reliable extraction of x-ray refraction and dark-field signals with a large field of view, multi-modal scanning system at spectral energies up to 150 kVp

To cite this article: T Partridge *et al* 2024 *J. Phys. D: Appl. Phys.* **57** 175104

View the [article online](#) for updates and enhancements.

You may also like

- [Application of pipeline leakage detection based on distributed optical fiber acoustic sensor system and convolutional neural network](#)
Yuxing Duan, Lei Liang, Xiaoling Tong *et al.*
- [On the influence of humidity on the breakdown strength of air—with a case study on the PDIV of contacting enameled wire pairs](#)
R Färber, O Šefl and C M Franck
- [Structural Characterization of Membrane-Electrode-Assemblies in High Temperature Polymer Electrolyte Membrane Fuel Cells](#)
Merit Bodner, Janet Jonna Bentzen, Vedrana Andersen Dahl *et al.*

PRIME
PACIFIC RIM MEETING
ON ELECTROCHEMICAL
AND SOLID STATE SCIENCE




HONOLULU, HI
Oct 6–11, 2024

Abstract submission deadline:
April 12, 2024

Learn more and submit!

Joint Meeting of
The Electrochemical Society
•
The Electrochemical Society of Japan
•
Korea Electrochemical Society

Reliable extraction of x-ray refraction and dark-field signals with a large field of view, multi-modal scanning system at spectral energies up to 150 kVp

T Partridge^{1,*} , A Astolfo¹, I Buchanan¹, G K Kallon¹, P R T Munro¹, C K Hagen¹, M Endrizzi¹ , D Bate² and A Olivo¹ 

¹ Department of Medical Physics and Biomedical Engineering, UCL, London WC1E 6BT, United Kingdom

² Nikon X-Tek Systems Ltd, Tring, Herts HP23 4JX, United Kingdom

E-mail: tom.partridge@ucl.ac.uk

Received 4 August 2023, revised 8 January 2024

Accepted for publication 19 January 2024

Published 5 February 2024



Abstract

Multi-modal x-ray scanning allows the simultaneous acquisition of attenuation, refraction and ultra-small angle scattering or dark field images. While many examples of multi-modal x-ray scanning exist in the literature, extension to high x-ray energy, necessary to investigate dense and high-Z materials, still poses challenges. We present the investigation of attenuation, refraction and dark field images taken at 90, 120 and 150 kVp, using a scanning, large field of view multi-modal imaging system. Increases in tube voltage reduce both contrast and signal to noise but still produce satisfactory results suitable for quantitative analysis. On top of benchmarking against phantoms made of known materials, we illustrate this by scanning a 9 V PP3 battery; a highly absorbing sample which causes photon starvation at lower energies.

Keywords: x-ray, phase contrast, multi-modal, high energy

1. Introduction

Recent years have seen an increased interest in so-called multi-modal x-ray imaging [1]; acquiring conventional attenuation images at the same time as phase and ultra-small angle scattering, also referred to as dark field [2]. Following early demonstrations using crystal-based systems at synchrotrons [3], this latter signal has become available also in standard labs using grating interferometry [4], edge-illumination (EI) [5] or methods using alternative beam modulators [6–8]. The interaction is often explained by means of the complex refractive index,

$n(E) = 1 - \delta(E) + i\beta(E)$, where β describes the attenuation and δ , the unit decrement of the real component, describes the phase [9]. Interest in acquiring phase images continues to be driven by the fact that δ is generally much greater than β , and decreases with energy at a lower rate. These attributes mean that phase images could still provide high contrast images when reduced dose or increased material penetration is important. As such, the method has been developed for several fields including, but not limited to, medical imaging [10], security [11], industrial testing [12] and materials science [13]. In particular, dark field imaging has reached the *in vivo* stage in lung imaging [10], and attempts are underway to implement grating interferometers on a clinical CT gantry [14].

Ramping multi-modal methods up to higher x-ray energies is essential to target higher Z, thicker and denser materials, which includes some of the key applications mentioned above. For example the study on *in vivo* lung imaging is conducted at 70 kVp as a ‘reasonable compromise between interferometer

* Author to whom any correspondence should be addressed.



Original content from this work may be used under the terms of the [Creative Commons Attribution 4.0 licence](https://creativecommons.org/licenses/by/4.0/). Any further distribution of this work must maintain attribution to the author(s) and the title of the work, journal citation and DOI.

performance and x-ray transmission' [15], while the CT gantry implementation was developed at 80 kVp [14]; both these important studies would benefit at least from the option of extending scans to higher x-ray energies. While experimentation exists on higher-energy multi-modal x-ray imaging at synchrotrons [16, 17], translation to laboratory x-ray sources still needs to be developed further. At the moment of writing, we are only aware of two lab-based studies utilising tube voltages of 120 kVp [11, 18], both somewhat lacking in quantitative signal analysis/benchmarking. In this study we consider the effect of tube voltages of 90, 120 and 150 kVp on the multi-modal image contrast and signal to noise ratio (SNR). We analyse the signal behaviour versus increasing spectral energy and, at least for refraction, we benchmark the experimental results against an established theoretical model. We also demonstrate with a practical example how higher energy x-rays are essential to image high Z materials, such as batteries.

2. Materials and methods

This work uses EI to generate phase contrast, where gold masks are placed before and after the sample to translate changes of phase into changes in intensity. The method has been in use for over 15 yr and applied to explosive detection [11], materials inspection [13] and a range of other areas, some of which are summarised in a recent review [19]. Figure 1 explains the EI principle where a sample scanned across the masks causes deviations of the x-ray beamlets, resulting in an increased or decreased signal arriving at the detector depending on the phase change. Prior to scanning, an illumination curve (IC) is acquired without a sample present by moving the position of the sample mask, an example is shown in figure 1(b). The shape of the IC is described by a normalised Gaussian, and subsequent deviations caused by sample scanning can then be treated as a perturbation to this Gaussian, with attenuation described by a reduction in integral, phase by a shift of the centre and scattering by an increase in the width of the Gaussian. In the description based on the complex refractive index, the scattering can thus be described as phase shifts at a sub-aperture resolution. To obtain all modalities, images must be taken at a minimum of three positions on the IC. These are typically taken at peak of the IC and at the half height positions on both sides (where the phase shift is seen as 'inverted' from one side to the other). In practice, further points are typically taken on the IC, including in the tails of the curve to improve scattering sensitivity [20]. In this study we made use of asymmetric pre-sample masks [21], which simultaneously sample 5 points of the IC without the need to adjust the mask position. This is achieved by taking a regularly spaced sample mask and sequentially adjusting neighbouring apertures by a small amount in groups of 5.

As a result, each point of this 5-pattern asymmetric pre-sample mask sees a different illumination level [22]. To generate images, detector columns corresponding to the same misalignment from the symmetric case are grouped together and

compared against the IC. In previous work we found that crosstalk between neighbouring apertures is best accounted for by using a five Gaussian IC described by [22]:

$$f_{IC}(x) = \sum_{i=1}^5 \frac{a_{1i}}{\sqrt{2\pi} a_{3i}} e^{-\frac{1}{2} \frac{(x-a_{2i})^2}{a_{3i}}} + a_4 \quad (1)$$

where x is the pre-sample mask lateral position, and i is the pixel index. The fitting parameters a_{1i} , a_{2i} , and a_{3i} are the amplitude, centre position and width of the i th Gaussian, respectively, while a_4 is the offset describing x-ray transmission through the gold of the mask. On addition of a sample to the field of view, it is then described by a perturbation to the IC function of:

$$f_{sample}(x) = \sum_{i=1}^5 \frac{a_{1i}s_1}{\sqrt{2\pi} (a_{3i} + s_3)} e^{-\frac{1}{2} \frac{(x-a_{2i}-s_2)^2}{a_{3i}+s_3}} + a_4s_4 \quad (2)$$

where s_1 , s_2 , and s_3 are the transmission, refraction and scattering, respectively, while s_4 takes into account the sample's offset modulation.

The x-ray source used in this system was a COMET MXR-160HP/11, operated at 7.7, 5.8 and 4.6 mA for peak voltages of 90, 120 and 150 kVp respectively. The source has broad and fine focus modes of operation, with respective power and nominal focal spots of 1.8 kW and 1 mm, and 0.8 kW and 0.4 mm. In this experiment the fine focus mode was used as it gives rise to a higher flux density. A tuneable Huber slit was placed in front of the source to collimate the beam to an effective focal spot of 70 μm . The source was uncollimated in the vertical direction. Note this is done for geometrical reasons, namely to prevent excessive beamlet overlap at the detector mask, which could make their individual analysis (and therefore the retrieval) more difficult. We are therefore selecting a roughly $400 \times 70 \mu\text{m}^2$ strip from the central part of an approximately round 400 μm diameter source, which corresponds to around 22% of the total source area, on the low-end side of the 0.2–0.4 open fraction range commonly used for G0 gratings [23]. It should also be noted that we have recently shown equivalent results with a 100 μm slit opening, corresponding to 32% of the source area being used [22], and that sources with an inherent 70–100 μm spot and much higher power are also common [24–26]. However, we note that it is also true that larger fractions would be unused if sources with a larger focal spot were utilised initially. In terms of spatial coherence, this remains negligible also after the introduction of the mask, as it ranges from approximately 0.7 μm at the highest spectral energy (150 kV) to 0.9 μm at the lowest (90 kV), approximately two orders of magnitude smaller than typical mask periods (see below). The setup can be seen in figure 1(c). A single photon counting Xcounter (XC-FLITE FX2) CdTe CMOS detector was employed, with 2048×128 square pixels measuring 100 μm in length, placed 2.1 m from the x-ray source. The detector is divided into 16 groups of 128 rows of pixels, resulting in a slight variation in detector response between the groups, adding to the striping seen in the example images of figure 2. Pre-sample and detector masks were manufactured by Microworks by electroplating 300 μm of gold on a 1 mm thick

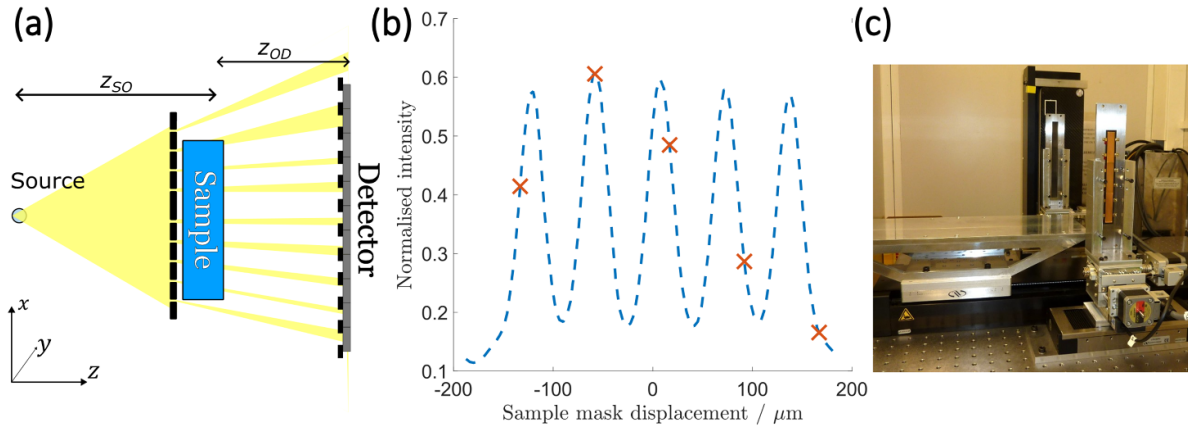


Figure 1. Edge-illumination principle and experimental setup: (a) a top-down view of the experiment showing the asymmetric splitting of the source into beamlets by the pre-sample mask and recording the counts at the detector. Inclusion of a sample causes a deviation of the beamlets, and in combination with the detector masks results in changes in the magnitude of x-rays reaching the detector. (b) An example illumination curve acquired by translation of the pre-sample mask, altering the counts incident on the detector. The crosses indicate common positions to sample the illumination curve for our asymmetric-mask EI experiment, though any points can be acquired. (c) A photo of the experimental setup as seen from the source (not visible).

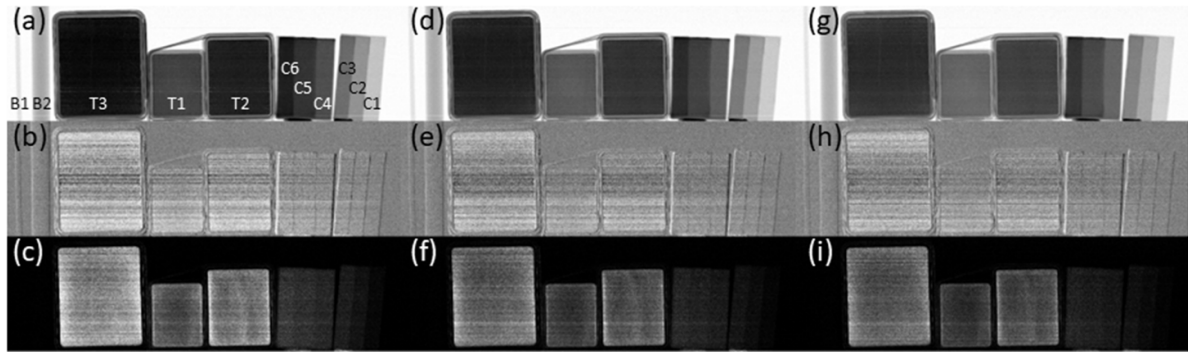


Figure 2. Example images at 90, 120 and 150 kVp (left, centre and right respectively) for attenuation: (a), (d) and (g), refraction: (b), (e), (h), and dark field: (c), (f) and (i). Colour scales were fixed for all three tube voltages to allow comparison. As shown on (a), attenuation and scatter are reported for the three boxes containing talcum powder (T1-3), with thicknesses 12, 18 and 24 mm respectively, and the six card thicknesses (C1-6), with thickness 10–60 mm respectively, while refraction is shown for the two PMMA bars (B1-2), with diameters 3 and 10 mm respectively.

graphite substrate. These were placed at 1.60 m and 2.06 m from the source, respectively. The detector mask was 20 cm tall and featured $128 \times 28 \mu\text{m}$ wide apertures (one per detector pixel), with a regular period of $98 \mu\text{m}$. The pre-sample mask was 15 cm tall and featured $128 \times 21 \mu\text{m}$ wide apertures arranged in a 5-way asymmetric pattern. This was achieved by sequentially altering a regularly spaced $75 \mu\text{m}$ mask in groups of 5 by $-20.8 \mu\text{m}$, $-10.4 \mu\text{m}$, $0 \mu\text{m}$, $10.4 \mu\text{m}$ and $20.8 \mu\text{m}$ [22]. As a general note, the relatively large size of the mask apertures allows reaching thicker gold layers without requiring excessively high aspect ratios. The masks were mounted on Newport linear translators for movement along and across the optical axis and on a Kohzu manufactured cradle for rotation around the optical axis. Scanning of the samples across the field of view was achieved using an additional Newport translator, such that the largest possible field of view is 20×50 cm. The exposure time per frame was 1 s. During acquisitions, the talc, paper and acrylic rods were scanned at 0.32, 0.40 and

0.40 mms^{-1} with corresponding times for the 21 cm length scan of approximately 11, 9 and 9 min, for energies of 90, 120 and 150 kVp respectively. The battery was scanned over 4 cm and performed at 0.08 mms^{-1} , giving scanning times of approximately 8 min.

The samples studied, as labelled in figure 2(a), included three boxes containing talcum powder (T1-3) with thicknesses of 12, 18 and 24 mm, six card step wedges (C1-6) with thicknesses of 10–60 mm, and two poly(methyl methacrylate) (PMMA) bars (B1-2) with diameters of 3 and 10 mm. Talcum powder and card were known to give strong scattering responses (the former had been shown to push the system range) and so were used for attenuation and scattering values, while the PMMA rods were used to measure the refraction signal. Quantitative measurements were taken over as large an area as possible with 113 256 (286×396) pixels considered for each box, 21 361 (41×521) pixels for the paper, and 621 rows for the rods. The battery scanned was a standard PP3 9 V 6LP3146 alkaline battery.

To compare refraction results against theoretical predictions, two-dimensional simulations were conducted using a wave-optics model, which calculates image profiles by numerically solving the Fresnel/Kirchhoff diffraction integral. This applies the effects of finite source size and detector resolution through convolutions [27]. To reproduce full multi-modal images a three-dimensional Monte–Carlo based approach was used based on an adaptation of McXtrace [28–30], which can generate multiple scattering events from randomly distributed particles smaller than the system’s spatial resolution.

3. Results and discussion

Example images extracted according to equation (2) are shown in figure 2 for the three energies considered. The tube current and scanning speeds were altered with each energy to give a constant photon count, so that the statistics were comparable. The detector utilises a low-energy threshold of 25 keV, thus photons whose energies are below this are not counted. However, this threshold is known to fluctuate slightly between both the rows and frames recorded, which, along with the varied detector response from each group of 128-pixel rows, leads to the horizontal striping seen in the images that is not removed by flat fielding.

It is clear from figure 2 that the contrast in each channel is different, the PMMA bars for example being absent from the scattering images due to their homogeneous internal structure. A close-up of the refraction image of just the PMMA bars is shown in figure 3. The positive and negative phase shifted edges are particularly evident on the 10 mm rod.

Areas of the images were extracted to quantify the change in both contrast and SNR, shown in figures 4 and 5 respectively. The contrast for attenuation, refraction and scattering are defined as:

$$C_{\text{ATN}} = \frac{|\bar{x}(\text{obj}) - \bar{x}(\text{air})|}{\bar{x}(\text{air})} \quad (3a)$$

$$C_{\text{REF}} = \frac{\text{Peak}_+ - \text{Peak}_-}{\text{Peak}_+ + \text{Peak}_-} \quad (3b)$$

$$C_{\text{SCA}} = \overline{\text{obj}} \quad (3c)$$

while SNRs for each channel are defined by:

$$\text{SNR}_{\text{ATN}} = \frac{|\bar{x}(\text{obj}) - \bar{x}(\text{air})|}{\sigma(\text{air})} \quad (4a)$$

$$\text{SNR}_{\text{REF}} = \frac{\text{Peak}_+ - \text{Peak}_-}{\sigma_{\text{air}}} \quad (4b)$$

$$\text{SNR}_{\text{SCA}} = \frac{\bar{x}_{\text{obj}} - \bar{x}_{\text{air}}}{\sigma_{\text{air}}} \quad (4c)$$

Considering figure 4, the contrast drops with increasing energy in all three channels, as can already be seen in figures 2 and 3, but features remain detectable at all considered spectral energies. The error bars in figure 4 show the standard deviation over the areas of interest chosen. An additional note here is that, while attenuation and refraction error bars quantify the

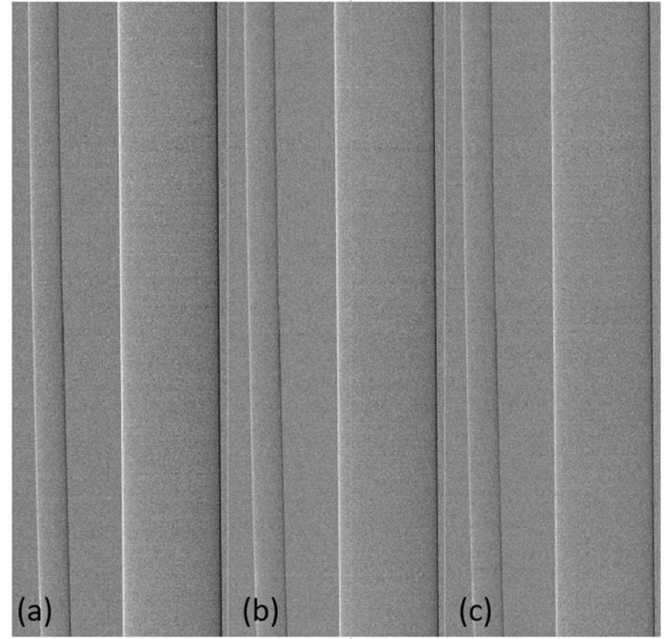


Figure 3. Zoomed in region of refraction image of the PMMA rods at (a) 90 kVp, (b) 120 kVp and (c) 150 kVp. The strong edge effects are noticeable on both rods though they decrease with peak energy.

variance of the measurement, it is believed those of scattering also include the inherent difference from features of the material sub-structure i.e. of different textures, which is why the paper and talc have different error bar magnitudes at similar scattering values as in talc 12 mm and paper 60 mm.

The acceptable loss of sensitivity with increasing energy is further supported by the SNR measurements shown in figure 5, where the drop with greater x-ray energy is not sufficient to plunge the considered detail below the visibility threshold.

To check the refraction values recorded in the experiment against theoretical values, simulations were performed at all energies using a previously tested wave optics model [27]. The profiles across the 10 mm rod can be seen in figure 6. The unretrieved profiles are shown in figures 6(a)–(c) and display a good agreement from simulation to experiment at all three energies. The expected edge spikes are not as significant in the raw data due to the averaging of several rows to create the profile. The retrieved refraction profiles, figures 6(d)–(f) also show the experiment to be well predicted by the established model, showing no loss in reliability in experimental data as energy is increased, and that delta values matching the theoretical ones are retrieved.

Returning to figure 4, this also highlights some deviation in the expected linearity of the scattering response vs. sample thickness [31] for both the talcum powder and paper—this is due to beam hardening [32]. To probe the break from linearity further, we exploited the used detector’s mid-threshold, which allows for dual energy scanning. The mid-threshold position was chosen to give approximately equal numbers of photons in the high and low energy bins. Figure 7 shows the attenuation and scattering contrasts for the paper at total, low and high

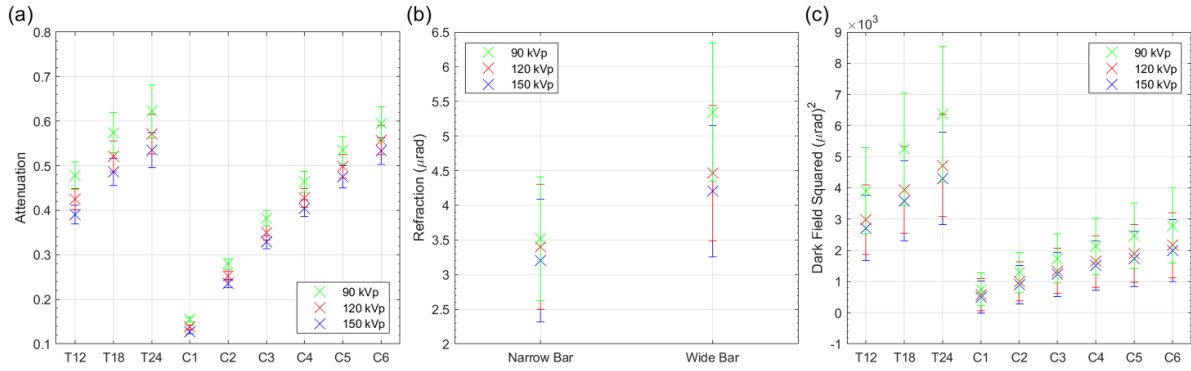


Figure 4. Retrieved quantitative contrast values for: (a) attenuation, (b) refraction and (c) dark field. Attenuation and scatter are reported for the three boxes containing talcum powder and the six paper thicknesses, while refraction is shown for the two PMMA rods.

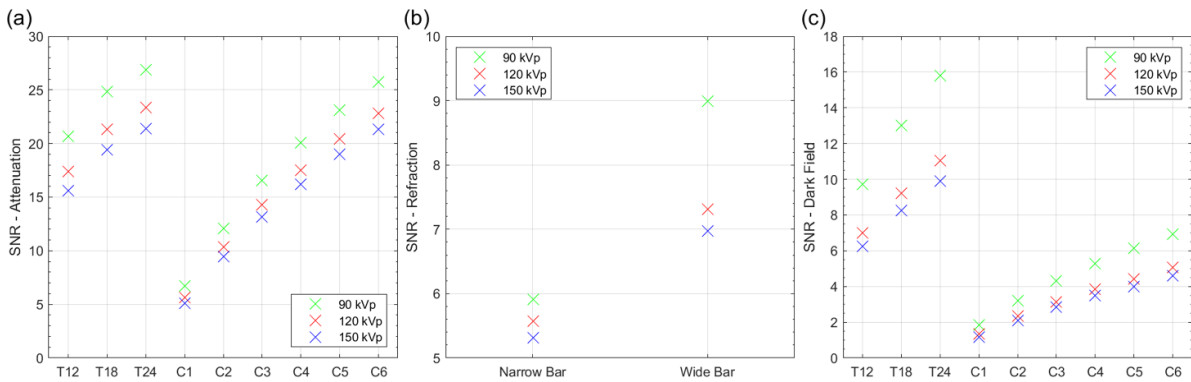


Figure 5. Retrieved SNR values for: (a) attenuation, (b) refraction and (c) dark field. Attenuation and scatter are reported for the three boxes containing talcum powder and the six paper thicknesses, while refraction is shown for the two PMMA rods.

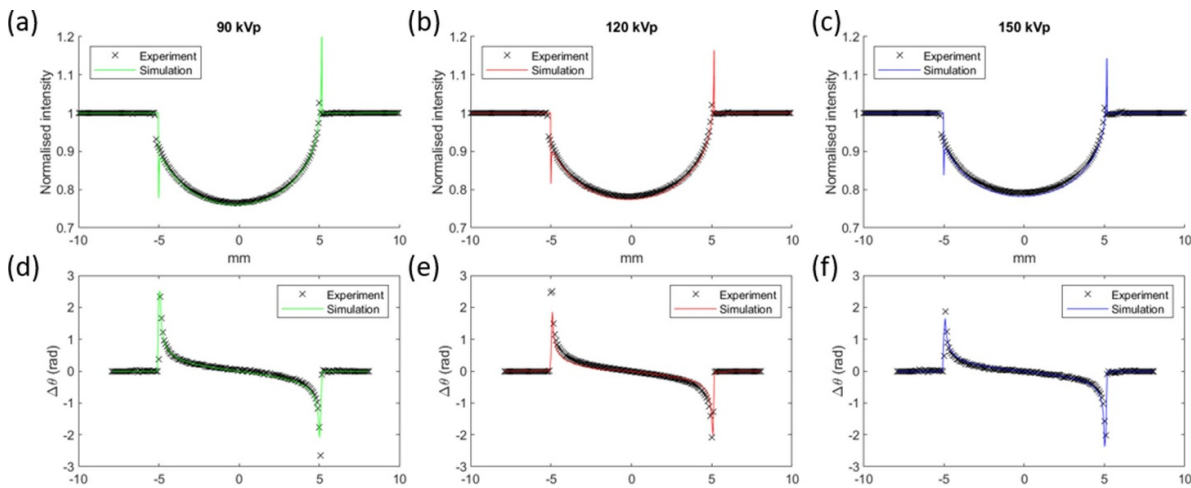


Figure 6. Raw and refraction profiles for the 10 mm acrylic rod at all three energies with (a)–(c) showing raw image profiles and (d)–(f) showing retrieved image profiles.

energy. The expected beam hardening induced deviation from linearity of the low energy scattering with increasing thickness is observed; however, given the reduced attenuation from the higher energy x-rays, the high energy bin is much less affected, and so displays an excellent linear response, figure 7(f).

In both contrast and SNR measurements (figures 4 and 5), a larger jump exists from 90 to 120 kVp than from 120 to

150 kVp. To explore this further, Monte–Carlo simulations of the setup for the paper samples were conducted. It should be noted that the simulations were designed to test the spectral response and not replicate the quantitative dark field of paper; making use of a simplified paper model using spheres with an estimated refractive index the rather than the non-uniform fibres we’d expect to find in a real paper sample. The

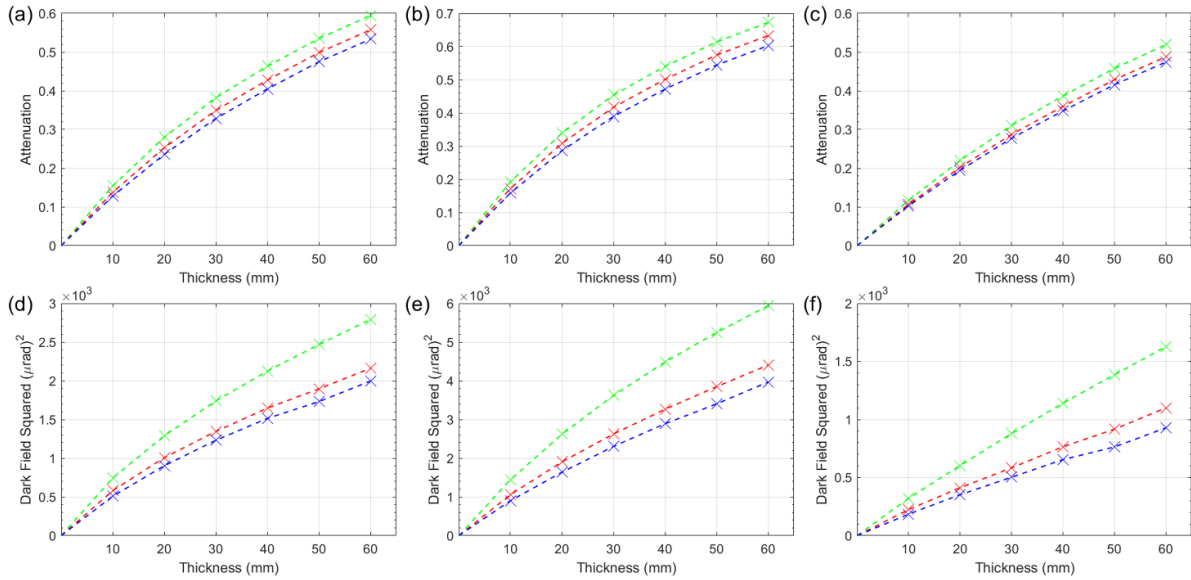


Figure 7. Dual energy results for the paper attenuation with (a) total, (b) low, and (c) high energy, and dark field (d) total, (e) low, and (f) high energy. Results corresponding to different peak energies are shown in different colours, namely green, red, and blue for 90, 120 and 150 kVp respectively.

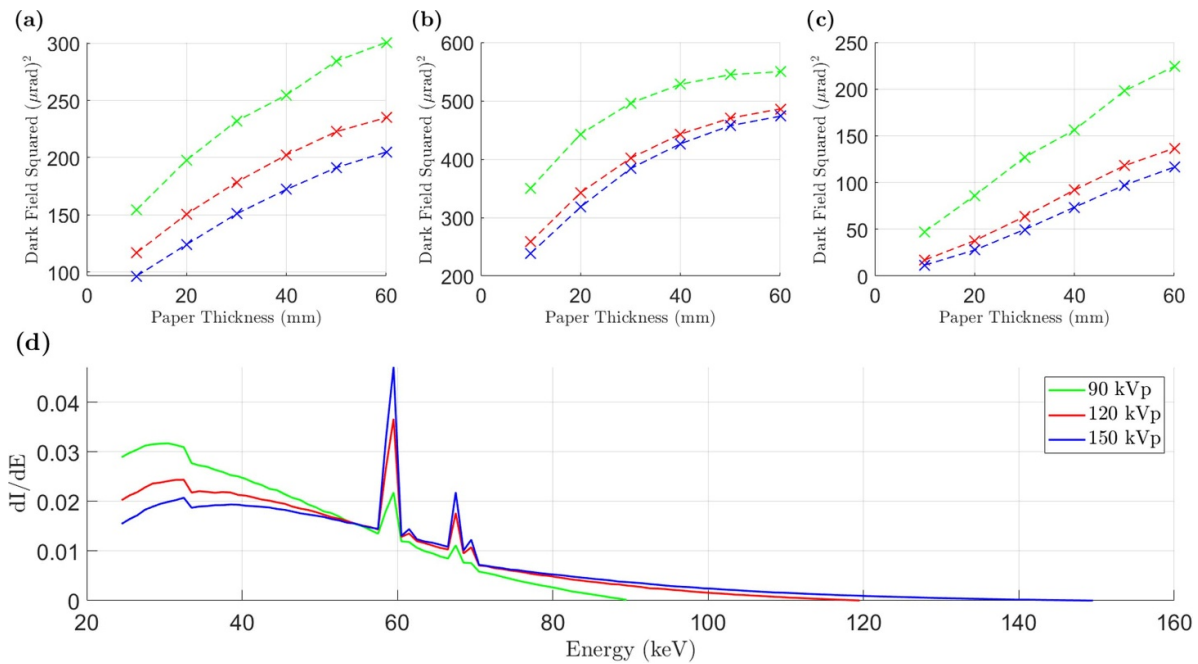


Figure 8. Scattering results from Monte–Carlo simulation of all paper thicknesses at the three energies acquired for (a) total energy, (b) low energy, and (c) high energy. (d) Predicted x-ray spectra including 1 cm paper and the detector CdTe response using tube voltages of 90, 120 and 150 kVp. In all figures different peak energies are shown in different colours, namely green, red, and blue for 90, 120 and 150 kVp respectively.

results of simulations for total, low and high energy scattering are shown in figures 8(a)–(c) respectively. Although, as already mentioned, reproducing the exact numerical values for the scattering signal would require an exact knowledge of the paper’s microstructure, we note that the general trend observed in the experimental results of figures 7(d)–(f) is reproduced. Namely, the non-linear response from beam hardening in the

total and low energy channels is exhibited alongside its rectification in the high energy one, and the reduced jump in signal from 120 to 150 kVp is also observed. This latter effect is thought to be due to the change in spectra with increasing tube voltage, which causes the effective δ of the samples to decrease by smaller proportional amounts with each increase in kVp. The predicted x-ray spectra (normalised to the same

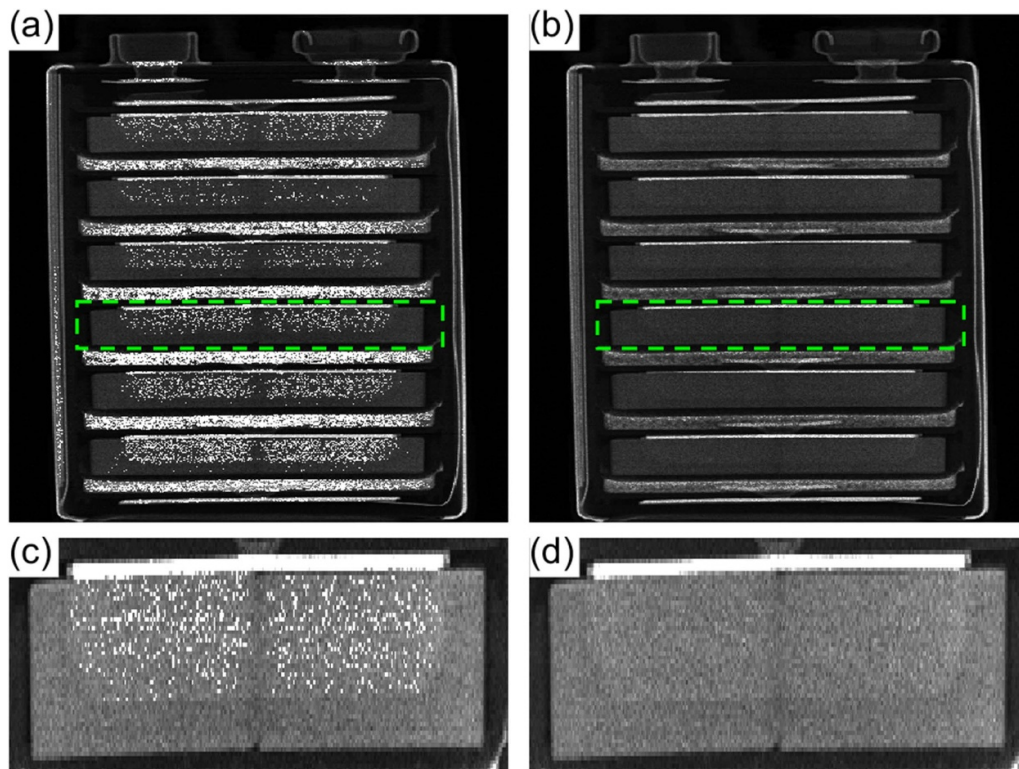


Figure 9. Retrieved dark-field images of a 9 V PP3 battery at (a), (c) 90 kVp and (b), (d) 150 kVp.

total area to better highlight the relative of each energy component) are shown in figure 8(d), where it can be seen the enhanced K edges of the Tungsten source at higher voltages results in a different mix of energies incident on the sample. This is further supported by the different relative proportional changes seen in the low and high energy scattering channels in figures 7(e) and (f), when comparing 90–120 kVp and 120–150 kVp. Investigating this further would require higher energy and/or filtered beam experiments and lies beyond the scope of the present work.

Dark-field images of a 9 V PP3 battery retrieved from scans taken at 90 and 150 kVp are shown in figure 9. As can be seen, the insufficient beam penetration leads to multiple failures in the Gaussian fitting procedure used to retrieve the dark-field signal. This is due to insufficient statistics, particularly evident (as bright dots) in the zoomed-in inset of panel (a).

Conversely, when the accelerating voltage is ramped up to 150 kVp the problem is solved, practically eliminating the ‘failing’ pixels and highlighting the more scattering parts of the cathode in line with previous experiments conducted at synchrotrons. We note that the attenuation of the densest parts of the 9 V PP3 battery at 90 kVp is approximately 99.8%, which makes it difficult to overcome photon starvation simply by e.g. increasing the exposure time (please also note that the mA’s had to be lowered when increasing the kV’s from 90 to 150). Alongside the fact that, even where possible, increasing the exposure time may not be convenient, this provides a clear example of the necessity of imaging certain samples at higher x-ray energies.

4. Conclusions

Multi-modal scans were taken of a number of materials with tube voltages of 90, 120 and 150 kVp. This increase in x-ray energy has been shown to reduce contrast and SNR in all channels, but the results are still of high enough quality such that scanning at these greater energies could be of significant benefit for many areas of study where increased penetration, and potentially reduced dose (see e.g. [33]), are important. As far as the refraction signal is concerned, experiments were replicated using wave optics simulations, the results of which matched those observed in experiment. The larger jump seen in contrast in all modalities from 90 to 120 kVp than from 120 to 150 kVp was also reproduced using Monte–Carlo simulations. By exploiting the dual-energy capabilities of the used detector, the expected linearity of the scatter signal vs. sample thickness was observed at higher energies, confirming that deviations at lower energies are due to beam hardening. When applied to a high Z material, namely a 9 V alkaline battery, the increasing tube voltage was shown to reduce artefacts caused by photon starvation, resulting in improved retrieved images and more reliable scans. This work shows that multi-modal x-ray phase contrast is both of benefit and quantitative at higher energies, opening up the field to higher Z materials.

Data availability statement

The data cannot be made publicly available upon publication because they contain commercially sensitive information. The

data that support the findings of this study are available upon reasonable request from the authors.

Acknowledgments

This work is supported by EPSRC (Grant EP/T005408/1). A O is supported by the Royal Academy of Engineering under their Chairs in Emerging Technologies scheme (CiET1819/2/78).

ORCID iDs

T Partridge  <https://orcid.org/0000-0001-8135-2099>

M Endrizzi  <https://orcid.org/0000-0002-7810-2301>

A Olivo  <https://orcid.org/0000-0002-7150-2951>

References

- [1] Wernick M N, Wirjadi O, Chapman D, Zhong Z, Galatsanos N P, Yang Y, Brankov J G, Oltulu O, Anastasio M A and Muehleman C 2003 Multiple-image radiography *Phys. Med. Biol.* **48** 3875–95
- [2] Pagot E, Cloetens P, Fiedler S, Bravin A, Coan P, Baruchel J, Hartwig J and Thomlinson W 2003 A method to extract quantitative information in analyzer-based x-ray phase contrast imaging *Appl. Phys. Lett.* **82** 3421
- [3] Rigon L, Besch H-J, Arfelli F, Menk R-H, Heitner G and Plochow-Besch H 2003 A new DEI algorithm capable of investigating sub-pixel structures *J. Phys. D: Appl. Phys.* **36** A260000–112
- [4] Pfeiffer F, Bech M, Bunk O, Eikenberry E F, Brönnimann C, Grünzweig C and David C 2008 *Nat. Mater.* **7** 134
- [5] Endrizzi M, Diemoz P C, Millard T P, Jones J L, Speller R D, Robinson I K and Olivo A 2014 Hard x-ray dark-field imaging with incoherent sample illumination *Appl. Phys. Lett.* **104** 024106
- [6] Morgan K S, Paganin D M and Siu K K W 2011 Quantitative single-exposure x-ray phase contrast imaging using a single attenuation grid *Opt. Exp.* **19** 19781–9
- [7] Zanette I, Zhou T, Burvall A, Lundström U, Larsson D H, Zdora M, Thibault P, Pfeiffer F and Hertz H M 2014 Speckle-based x-ray phase-contrast and dark-field imaging with a laboratory source *Phys. Rev. Lett.* **112** 253903
- [8] Berujon S, Wang H and Sawhney K 2012 x-ray multimodal imaging using a random-phase object *Phys. Rev. A* **86** 063813
- [9] Born M and Wolf E 1999 *Principles of Optics: Electromagnetic Theory of Propagation, Interference and Diffraction of Light* 7th edn (Cambridge University Press)
- [10] Willer K *et al* 2021 X-ray dark-field chest imaging for detection and quantification of emphysema in patients with chronic obstructive pulmonary disease: a diagnostic accuracy study *Lancet Digit. Health* **3** e733–44
- [11] Partridge T, Astolfo A, Shankar S S, Vittoria F A, Endrizzi M, Arridge S, Riley-Smith T, Haig I G, Bate D G and Olivo A 2022 Enhanced detection of threat materials by dark-field x-ray imaging combined with deep neural networks *Nat. Commun.* **13** 4651
- [12] Revol V, Jerjen I, Kottler C, Schütz P, Kaufmann R, Lüthi T, Sennhauser U, Straumann U and Urban C 2011 Sub-pixel porosity revealed by x-ray scatter dark field imaging *J. Appl. Phys.* **110** 044912
- [13] Shoukroun D, Massimi L, Iacoviello F, Endrizzi M, Bate D, Olivo A and Fromme P 2020 Enhanced composite plate impact damage detection and characterisation using x-ray refraction and scattering contrast combined with ultrasonic imaging *Composites B* **181** 107579
- [14] Viermetz M *et al* 2022 Dark-field computed tomography reaches the human scale *Proc. Natl Acad. Sci. USA* **119** e2118799119
- [15] Sauter A P *et al* 2019 Optimization of tube voltage in x-ray dark-field chest radiography *Sci. Rep.* **9** 8699
- [16] Ruiz-Yaniz M, Zanette I, Rack A, Weitkamp T, Meyer P, Mohr J and Pfeiffer F 2015 x-ray refractive-index measurements at photon energies above 100 keV with a grating interferometer *Phys. Rev. A* **91** 033803
- [17] Ruiz-Yaniz M, Koch F, Zanette I, Rack A, Meyer P, Kunka D, Hipp A, Mohr J and Pfeiffer F 2015 x-ray grating interferometry at photon energies over 180 keV *Appl. Phys. Lett.* **106** 151105
- [18] Kimura K, Sun M, Ueda R, Wu Y, Pan H and Momose A 2021 High-energy x-ray phase tomography using grating interferometer with structured anode x-ray source *Proc. SPIE* **11840** 118400K–1
- [19] Olivo A 2021 *J. Phys.: Condens. Matter* **33** 363002
- [20] Massimi L, Partridge T, Astolfo A, Endrizzi M, Hagen C K, Munro P R T, Bate D and Olivo A 2021 Optimisation of multi-point phase retrieval in edge illumination x-ray imaging *Med. Phys.* **48** 5884–96
- [21] Endrizzi M, Astolfo A, Vittoria F A, Millard T P and Olivo A 2016 Asymmetric masks for laboratory-based x-ray phase-contrast imaging with edge illumination *Sci. Rep.* **6** 25466
- [22] Astolfo A, Buchanan I, Partridge T, Kallon G K, Endrizzi M, Hagen C K and Munro P R T 2022 The effect of a variable focal spot size on the contrast channels retrieved in edge-illumination x-ray phase contrast imaging *Sci. Rep.* **12** 3354
- [23] Pfeiffer F, Weitkamp T, Bunk O and David C 2006 Phase retrieval and differential phase-contrast imaging with low-brilliance x-ray sources *Nat. Phys.* **2** 258–61
- [24] Saghmanesh S, Aghamiri S M, Kamali-Asl A and Yashiro W 2017 *Phys. Med. Biol.* **62** 7394
- [25] Eckermann M, Töpperwien M, Robisch A-L, van der Meer F, Stadelmann C and Salditt T 2019 Phase-contrast x-ray tomography of neuronal tissue at laboratory sources with sub-micron resolution *Proc. SPIE* **11112** 111120R
- [26] Kalasová D, Zikmund T, Pina L, Takeda Y, Horvath M, Omote K and Kaiser J 2020 Characterization of a laboratory-based x-ray computed nanotomography system for propagation-based method of phase contrast imaging *IEEE Trans. Instrum. Meas.* **69** 1170–8
- [27] Vittoria F A, Diemoz P C, Endrizzi M, Rigon L, Lopez F C, Dreossi D, Munro P R T and Olivo A 2013 Strategies for efficient and fast wave optics simulation of coded-aperture and other x-ray phase-contrast imaging methods *Appl. Opt.* **52** 6940–7
- [28] Bergback Knudsen E *et al* 2013 *J. Appl. Cryst.* **46** 679–96
- [29] Millard T P, Endrizzi M, Diemoz P C, Hagen C K and Olivo A 2014 Monte Carlo model of a polychromatic laboratory based edge illumination x-ray phase contrast system *Rev. Sci. Instrum.* **85** 053702
- [30] Buchanan I *et al* 2023 Direct x-ray scattering signal measurements in edge-illumination/beam-tracking imaging and their interplay with the variance of the refraction signals *Appl. Phys. Rev.* **10** 041406

- [31] Endrizzi M, Vittoria F A, Rigon L, Dreossi D, Iacoviello F, Shearing P R and Olivo A 2017 X-ray phase-contrast radiography and tomography with a multiaperture analyzer *Phys. Rev. Lett.* **118** 243902
- [32] Yashiro W, Vagovic P and Momose A 2015 Effect of beam hardening on a visibility-contrast image obtained by x-ray grating interferometry *Opt. Exp.* **23** 23462–71
- [33] Diemoz P C *et al* 2016 A method for high-energy, low-dose mammography using edge illumination x-ray phase-contrast imaging *Phys. Med. Biol.* **61** 8750–61